I&EC research
Industrial & Engineering Chemistry Research

Open Access
This article is licensed under CC-BY 4.0

pubs.acs.org/IECR
Article

Effect of Thermal, Acid, and Alkaline Treatments over SAPO-34 and Its Agglomerated Catalysts: Property Modification and Methanol-to-Olefin Reaction Performance

Diego Zapater, Javier Lasobras, Naydu Zambrano, Idoia Hita, Pedro Castaño, Jaime Soler, Javier Herguido,* and Miguel Menéndez

Cite This: https://doi.org/10.1021/acs.iecr.3c03956
Read Online

ACCESS | Metrics & More | Article Recommendations | Supporting Information

ABSTRACT: SAPO-34 zeolite is one of the most well-studied methanol-to-olefin catalysts, with applications from laboratory to commercial scale. Here, we have studied the impact on the properties and performance of different modifications of a commercial zeolite, including thermal, acid, and alkaline treatments, along with its agglomeration with bentonite and alumina required in the technical catalyst. We prepared three zeolites and agglomerated them, making a total of seven materials, along with our benchmark catalyst. These were characterized and tested in a packed bed reactor. We analyzed the conversion, yield, and deactivation (coke) based on the effective acid site density ρ_{AS}* (a parameter correlating acid strength, density, and micropore volume). Thermal treatment increased the effective acid site density of the commercial zeolite by 60%, while only a 10% increase was found in the parent agglomerated catalyst. Acid etching increased the effective acid site density by 80%, while the basic treatment completely amorphized the framework of the zeolite. After agglomeration, the performance of the catalysts (by means of olefin production and deactivation) correlated with effective acid site density. The catalysts based on thermally and acid-treated zeolites performed best, while they had the lowest effective acid site density.

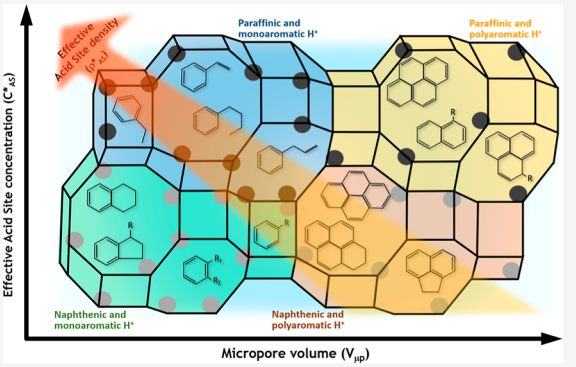

Downloaded via UNIV DE ZARAGOZA on February 5, 2024 at 10:09:51 (UTC).
See https://pubs.acs.org/sharingguidelines for options on how to legitimately share published articles.

1. INTRODUCTION

The methanol-to-olefin (MTO) process is a successful route to produce light olefins, specifically ethylene and propylene, from various resources including, but not limited to, natural gas, coal, and biomass. For all of those sources, as well as for the proper MTO process, methanol and dimethyl ether (DME) act as intermediates to olefin final production. Over the last 40 years, the MTO process has received a lot of attention because of the low cost of its raw materials and the value of its products.

Crystalline zeolites stand out as the best catalysts for the MTO process due to their unique shape selectivity, suitable acidity, and robust thermal and hydrothermal stabilities.[1−6] Among the available materials, silicoaluminophosphate (SAPO) zeolites, such as SAPO-34 (CHA framework), emerge as ideal catalysts for ethylene and propylene production. This is attributed to the strong shape selectivity provided by its 8 membered-ring structure with a small pore size (around 3.5 Å) connecting large cavities. This structural feature limits the diffusion of heavy and branched hydrocarbons, thereby increasing the selectivity to light olefins.[6,7]

SAPO-34 catalysts usually have a small particle size (ca. 2 μm), which makes it difficult to operate within packed bed reactors due to a large pressure drop. Agglomeration with other materials, such as clays and oxides, plays an important role in this because it allows to produce SAPO-34-based catalysts with bigger particle size, improved attrition resistance, and modified properties.[8−12]

Despite the very good performance provided by the CHA framework to produce light olefins, this structure also facilitates rapid coke formation and accumulation. As a result, catalyst performance declines rapidly, necessitating a paired regeneration process to maintain stability in long-term runs.[1,13−16] Based on the well-established dual cycle MTO reaction mechanism involving an olefin and a hydrocarbon pool, it is assumed that the main cause of deactivation is the transformation of the latter pool species into polycyclic aromatics. These aromatics remain trapped within the zeolite cavities, covering active sites and causing a pore blockage.[1,17−20] While highly condensed (and often insoluble) polyaromatics severely

Received: November 14, 2023
Revised: December 27, 2023
Accepted: December 28, 2023

ACS Publications
© XXXX The Authors. Published by American Chemical Society

worsen catalytic activity, methylated mono- and bicyclic aromatics are reported to be beneficial for the MTO reaction at precoked catalyst conditions.[21,22] This is usually a problem in offline coke analysis because it becomes difficult to distinguish between active and inactive (deactivating) species. Despite the complexity of this task, there are several strategies available to circumvent the very rapid coke formation in the MTO reaction. These strategies include water cofeeding,[15,23,24] the design of deactivation-resistant catalysts,[25] or catalyst modification through either incorporation of other metals or via thermal, acid, or basic treatments.[25−33] These last groups of modifications are of special interest because they are easy to perform and modify some of the most relevant characteristics of the materials (thermal stability, acid site distribution and strength, and elemental composition).

This work explores the last of these strategies by performing various physical and chemical modifications over a SAPO-34 zeolite and some of its agglomerated catalysts. The main goal is to enhance the understanding of how these modifications influence the properties of the solids, to confirm whether the prepared catalysts outperform the parent one in reaction within a packed bed, and to analyze if the coke species obtained at the end of reaction time are related with the initial physical−chemical properties of the fresh catalysts.

2. MATERIALS AND METHODS

This section describes SAPO-34 and parent catalyst modifications, their agglomeration processes, and characterization techniques. Additionally, a detailed portrayal of the catalytic tests performed with these compounds is also included.

2.1. Catalyst Preparation. The agglomerated catalysts used in this work are based on the SAPO-34 zeolite, which has been modified through thermal, acid, or alkaline treatments. We established HSAPO-34 (S sample) and a SAPO-34-based catalyst (AggC sample) as the starting samples that were later subjected to modifications, and the codes assigned to each material are summarized in Table 1. The catalyst (AggC) was prepared by agglomeration (wet impregnation) of HSAPO-34 (ACS Material, dp about 2 μm), bentonite (Sigma-Aldrich, dp < 100 μm), and alumina (Puralox, 45 < dp < 250 μm), with a weight ratio of 50/30/20. The first step was the mechanical mixing of the solid zeolite, clay, and alumina for 10 min. The mixture was humidified with 3 cm^3 of distilled water per gram of solid to obtain a wet paste, which was then mixed softly and dried, first at room temperature (25 °C) for 24 h and second at 120 °C for 12 h. Finally, the catalyst was calcined at 550 °C for 2 h at a 1 °C·min^{-1} rate. To ensure an acceptable pressure drop in the packed bed reactor, the catalyst was sieved to a desired particle size of 160−315 μm.[9,11,12,34−37] The treatments applied to the starting samples are the following:

Table 1. Coding for the Samples Used in This Work

starting sample	main treatment	additional treatment	code
SAPO-34			S
bentonite			B
SAPO-34	agglomeration		AggC
SAPO-34	thermal		S_T
		agglomeration	S_T_Agg
agglomerated catalyst	thermal		AggC_T
SAPO-34	acid		S_Ac
		agglomeration	S_Ac_Agg
SAPO-34	alkaline		S_Ba
		agglomeration	S_Ba_Agg

- Thermal treatment: the thermal treatment was carried out on the raw SAPO-34 (S) and agglomerated catalyst (AggC) samples. It consisted of two heating steps with a temperature slope of 2 °C·min^{-1} and a subsequent isotherm of 2 h. The first heating step was from 25 to 120 °C, while the second was from 120 to 900 °C.[30,38,39] The samples obtained from this treatment were designated as S_T and AggC_T for the SAPO-34 and catalyst-treated samples, respectively. Additionally, the sample S_T was agglomerated (following the same protocol previously described for the AggC sample) and labeled as S_T_Agg.
- Acid treatment: the acid treatment followed a modified procedure from Verboekend et al.[26] It was performed over the SAPO-34 sample (S) in a HCl solution (0.1 M) under magnetic stirring at 70 °C for 2 h (solid-to-liquid ratio of 67 g·L^{-1}). The S samples were then filtered, washed with distilled water (up to pH = 7.0), and dried at 65 °C for 12 h. A last step of calcination was performed at 550 °C for 5 h following a 5 °C·min^{-1} rate. The obtained treated zeolite and the catalyst prepared after its agglomeration were designated as S_Ac and S_Ac_Agg, respectively.
- Alkaline treatment: the basic treatment followed a modified procedure from Verboekend et al.[26] It was performed over the SAPO-34 sample (S) in a NaOH solution (0.2 M) under magnetic stirring at 70 °C for 30 min (solid-to-liquid ratio of 33 g·L^{-1}). Filtration, washing with distilled water (down to pH = 7.0), and drying at 65 °C for 12 h followed the initial step. Once dry, ionic exchange was performed in three consecutive steps in a NH_4NO_3 solution (0.1 M) for 18 h (solid-to-liquid ratio of 10 g·L^{-1}). Samples then underwent a calcination process at 550 °C for 5 h applying a temperature slope of 5 °C·min^{-1}. The resulting treated sample was labeled as S_Ba, and the resulting catalyst after agglomeration was designated as S_Ba_Agg.

2.2. Catalyst Characterization. The specific surface of the samples was measured by the static adsorption of CO_2 using a Quantachrome Autosorb iQ3 setup. Prior to analysis, the samples were degassed at 120 °C for 8 h. Particle size distribution of the agglomerated catalyst was determined by sieving. Composition and crystallinity were measured by X-ray fluorescence (XRF) (Thermo Electron ARL series, ADVANT/XP) and X-ray diffraction (XRD) (Panalytical Empyrean), respectively.

Brønsted acidity was measured by temperature-programed desorption (TPD) of NH_3. The sample was first saturated at 100 °C by an ammonia-saturated (at 0 °C) He gas stream and stabilized to remove physisorbed NH_3. In the desorption step, the temperature was increased following a 2 °C·min^{-1} slope. The setup was connected to a mass spectrometer (ThermoOnix ProLab), where the m/z = 16 signal was registered continuously. Acid sites were classified as "weak" (ASw) if their corresponding desorption peak is located <300 °C or as "strong" (ASs) if the peak appears at >300 °C. Brønsted acidity is one of the most relevant parameters in a zeolite for the MTO process. However, this acidity can be different regarding the

https://doi.org/10.1021/acs.iecr.3c03956
Ind. Eng. Chem. Res. XXXX, XXX, XXX−XXX

amount of acid sites and their strength. In order to account for this, a new parameter that simultaneously represents the strength and amount of acid sites can be defined as the effective acid site concentration (C_{AS}*, $mmol_{NH_3}·g^{-1}$).

$$C_{AS}^{*} = \sum_{i=1}^{n(\text{weak})} \left(\frac{T_i}{100} \cdot \frac{A_i}{A_{\text{weak}}} \right) + \sum_{j=1}^{m(\text{strong})} \left(\frac{T_j}{300} \cdot \frac{A_j}{A_{\text{strong}}} \right) \quad (1)$$

On the other hand, the distribution of these acid sites over the micropore structure of the samples is also relevant. If they form clusters, the adsorption−growth−desorption of hydrocarbon chains that takes place on them could lead to different products. Because of that, the effective acid site density is defined as the effective acid site concentration by units of micropore volume (ρ_{AS}*, $mmol_{NH_3}·cm^{-3}$)

$$\rho_{AS}^{*} = \frac{C_{AS}^{*}}{V_{\mu p}} \quad (2)$$

2.3. Catalytic Tests and Product Analysis. Catalytic tests were carried out only with the agglomerated samples because the parent or treated zeolite samples had a small particle size (dp ca. 2 μm) that caused a high pressure drop in the reactor and made it hard to operate.

An HPLC pump (LC-10AT, Shimadzu) fed the methanol (Fisher Scientific, purity >99.9%) and the water mixture to an evaporator, where it vaporized and mixed with nitrogen as a carrier gas. The gas mixture consisted of a 75% vol carrier gas and a 25% vol methanol−water (with a 1:1 molar ratio), which entered a cylindrical quartz reactor (30 cm high and 1 cm of internal diameter) equipped with a quartz plate acting as a gas distributor and a support of the catalyst bed. The reactor operated in a packed bed configuration with a catalyst load of 1 g and a W/F_{MeOH} of 22.7 g·h·mol^{-1}. The reactor was heated with an electric oven around it. The reaction temperature was set at 500 °C and controlled by a proportional integral derivative (PID) controller and a thermocouple located at the center of the catalyst bed. The pressure drop in the reactor was measured by using a pressure sensor (VAP 445, Digitron). All samples caused a pressure drop lower than 0.12 bar over the atmospheric pressure during operation. A pair of condensers downstream of the reactor and inside a cool bath (−15 °C) recovered water and unreacted methanol. A gas chromatograph (GC) (CP-3800, Varian) equipped with a capillary column (VF-624 ms, FactorFour) paired with a bubble meter was used to analyze permanent gases, while methanol and water were analyzed offline using a GC connected to a mass spectrometer (GC−MS QP2010, Shimadzu) provided with a capillary column (TRB-50.2 PONA, Teknokroma).

Carbon mass balance was calculated as

$$gC_{MeOH} = gC_{\text{permanent gases}} + gC_{MeOH} + gC_{\text{condensed}} \quad (3)$$

Conversion and product yield were defined as

$$X_{MeOH+DME} = \frac{(gC_{MeOH})_{in} - (gC_{MeOH} + gC_{DME})_{out}}{(gC_{MeOH})_{in}} \quad (4)$$

$$Y_i = \frac{(gC_i)_{out}}{(gC_{MeOH})_{in}} \quad (5)$$

For the results of the tests, we considered methanol (MeOH) and DME as reactives for conversion calculations because the latter is an intermediate in equilibrium from the first step in the MTO reaction (dehydration of methanol). The products of interest were light olefins, mainly ethylene (C_2H_4) and propylene (C_3H_6), while byproducts were methane (CH_4) and carbon monoxide (CO). We considered the latter relevant because of their believed relation with a competitive secondary mechanism found in previous works.[8,40] Considering other hydrocarbon products, only the agglomerated alkaline-treated catalyst showed a peak in GC corresponding to C_4 compounds. These were found at the first moments of reaction (sample time of 3 min), but their global yield was below a 2% in C weight basis. The amount of C_{5+} compounds was under the detection limit of the GC analysis, and no organic phase was found in the condensed phase. Finally, the catalyst was considered deactivated for olefin production when the yield of olefins decreased to 10%.

We calculate the mass balance globally and at each sampling time. For all experiments, it was over 89 and 87%, respectively. In the latter, we compared the total amount of measured coke with the missing mass balance and assigned it depending on that. It is reasonable to make this assumption because the global mass balance was close to 90% in all tests.

The deposited coke on the spent catalysts was classified as volatile and non-volatile and quantified through combined temperature-programed desorption and oxidation (TPD−TPO) in a TGA/DSC 1 STAR System by Mettler Toledo. The volatile coke was obtained from the initial stripping step, where the spent catalyst sample (ca. 10 mg) was subjected to sweeping under a He atmosphere (50 mL min^{-1}) in order to remove the adsorbed organic species, ramping up to 500 at 10 °C min^{-1} and maintaining an isotherm for 30 min. After that, the furnace was cooled down to 100 °C and the gas atmosphere was switched to air (50 mL min^{-1}) to start the oxidation step, from which we obtained the non-volatile coke. After sample stabilization for 10 min, a combustion ramp up to 800 °C at a 5 °C min^{-1} rate was performed.

In order to isolate the soluble coke, we applied a protocol reported in a previous work involving catalyst disaggregation using HF and a subsequent soluble coke extraction using CH_2Cl_2.[20] The ^{1}H nuclear magnetic resonance (NMR) analysis of the soluble coke was conducted in a Bruker AVANCE III 500 MHz spectrometer equipped with a Bruker 5 mm BBFO broad banded cryoprobe. For that purpose, the soluble coke was dissolved in 1 mL of methylene chloride-d2 (CD_2Cl_2, Thermo Scientific, 99.5%), and spectra were recorded by collecting 128 scans with a recycle delay time of 5 s using a 90° pulse sequence. Chemical shifts were adjusted using tetramethylsilane as an internal standard. The obtained spectra were processed using MestRenova V.14 software.

3. RESULTS AND DISCUSSION

This section includes the characterization of modified samples, catalytic performance of the agglomerated samples, coke formation and nature, and correlations between catalytic results and the properties of the treated catalysts.

SAPO-34 samples underwent thermal, acidic, and alkaline treatments. The characterization of the resulting samples followed the methods presented in Section 2.2. In addition, those agglomerated samples were tested in reaction, and their results show from the point of view of gaseous, liquid, and solid products. This section also provides a discussion about the results and a set of correlations between these results and the properties of the samples.

https://doi.org/10.1021/acs.iecr.3c03956
Ind. Eng. Chem. Res. XXXX, XXX, XXX−XXX

Table 2. Characterization of Parent Modified and Agglomerated SAPO-34 Samples

sample	micropore structure		acid site concentration		composition (wt %)				
	S_{CO_2} ($m^2 \cdot g^{-1}$)	$V_{\mu p}$ ($cm^3 \cdot g^{-1}$)	C_{ASw} ($mmol_{NH_3} \cdot g^{-1}$)	C_{ASs} ($mmol_{NH_3} \cdot g^{-1}$)	Si	Al	P	Fe	others
S	1272	0.38	6.53	8.97	5.9	23.1	20.8	0.6	49.6
B	93	0.04	2.61	0.08	29.9	14.8	3.7	3.2	48.4
AggC	663	0.18	5.31	3.61	12.5	22.2	11.1	1.0	53.2
S_T	937	0.29	0	8.23	5.9	22.9	20.6	0.7	49.9
S_T_Agg	580	0.17	2.55	2.66	12.5	22.3	10.5	1.0	53.7
AggC_T	267	0.09	3.91	2.12	12.3	22.6	10.5	1.0	53.6
S_Ac	1063	0.36	0	14.11	5.7	20.8	19.8	0.6	53.1
S_Ac_Agg	580	0.17	0	7.55	10.2	22.2	12.7	1.0	53.9
S_Ba	75	0.03	2.30	2.20	5.7	20.9	17.6	0.6	55.2
S_Ba_Agg	88	0.032	1.61	1.51	8.9	20.5	13.0	0.9	56.7

Table 3. Comparison of Theoretical and Experimental Acid Site Concentration for SAPO-34 Catalysts

sample	calculations	C_{ASw} ($mmol_{NH_3} \cdot g^{-1}$)	C_{ASs} ($mmol_{NH_3} \cdot g^{-1}$)	$C_{AStotal}$ ($mmol_{NH_3} \cdot g^{-1}$)
AggC	theoretical	4.11	4.52	8.63
	experimental	5.31	3.61	8.92
S_T_Agg	theoretical	0.85	4.15	5.0
	experimental	2.55	2.66	5.21
S_Ac_Agg	theoretical	0.85	7.09	7.94
	experimental	0	7.55	7.55
S_Ba_Agg	theoretical	2.0	1.14	3.14
	experimental	1.61	1.51	3.12

3.1. Sample Characterization. The results obtained from the characterization of the different catalysts are listed in Table 2. These include the micropore structure, acid site concentration, and composition. After the thermal, acid, and basic treatments, we observe significant modifications of the structural properties of the catalysts compared to those of the starting samples. The thermal treatment (S_T) reduces the micropore volume of the zeolite by 24.7%, which can be explained by the collapse of some pores caused by the thermal instability of the zeolite at the treatment temperatures. This crumble could lead to an enclosure of the structure and the subsequent lowering of CO_2 adsorption due to reduced accessibility. However, this treatment does not affect the micropore size distribution (Figure S1, Supporting Information) but only reduces the fraction of accessible micropores. The effect of the temperature could be the only cause for the reduction in micropore volume as long as it is the only modified parameter that affects the thermal stability of the zeolite.[39,41−46] The thermal treatment also modifies the total acid site concentration of the zeolite, which declines 47% from 15.5 to 8.23 mmol of $NH_3 \cdot g^{-1}$, and its distribution, which shifts the weak/strong site proportion from 42/58 to 0/100%. This can be a consequence of a combined effect of dehydroxylation and dehydration processes. The composition of the treated samples does not change because this modification is a physical process that does not add or remove any of the relevant elements of the SAPO-34 (Si, Al, P). When applied to the parent agglomerated catalyst (AggC), the thermal treatment infers a different effect. The AggC_T catalysts present 50.5% less micropore volume and 33% less total acidity, but its acid site distribution is maintained. In this case, the AggC_T catalyst is a physical mixture of three different components, zeolite (S), bentonite (B), and alumina (A), which could heat at a different rate due to its different heat capacity and transfer. This phenomenon can produce hot spots in the solid mixture and explain some of the results obtained regarding the structure and acidity.

The acid treatment has a different effect on the zeolite, reducing its micropore volume by 6.6%, its total acidity by 9%, and its Al and P contents from 23.1 and 20.8 to 20.8 and 19.8%, respectively. The main change in the S_Ac sample is a shift in its acid site nature from 42/58% weak/strong sites to 100% strong sites. There are three probable causes for this: the generation of framework OH^- groups, the reappearance of those from the structure blocked by cations in the parent sample, or the removal of some Al and P from the zeolite structure could cause a reduction in the electronegativity of some acid sites, which led to an uneven balance in the surface charge that increased their strength.[33,41,46,47] This latter cause is supported by other authors, who agree on the fact that the acid treatment selectively removes Al and P from the zeolite structure, and this effect is greater for Al because of its poor stability in acidic media compared with Si and P.

The alkaline treatment destroyed 95% of the micropore volume. The base amorphizes the framework and transforms the micropores (Figure S1, Supporting Information) into mesopores.[26,33] Treatment with NaOH also reduced the total acidity of the S_Ba sample by 71% from 15.5 to 4.50 mmol of $NH_3 \cdot g^{-1}$ and equilibrated the acid site distribution from 42/58 to 51/49% weak/strong sites. Furthermore, it also selectively removes Al and P, and a bigger proportion of the latter, in agreement with other authors who assign a greater sensitivity of P to base leaching.[26,33] In addition, this can explain the reduction in the acid site concentration because of the destruction of framework and structural OH^- groups.

As expected from a physical process like agglomeration, the properties of the agglomerated samples are generally a result of a weighted mean of those of their components (following the 50/30/20 mass ratio in the preparation). However, there were some discrepancies regarding the theoretical and measured acid site concentration of some samples, especially concerning

https://doi.org/10.1021/acs.iecr.3c03956
Ind. Eng. Chem. Res. XXXX, XXX, XXX−XXX

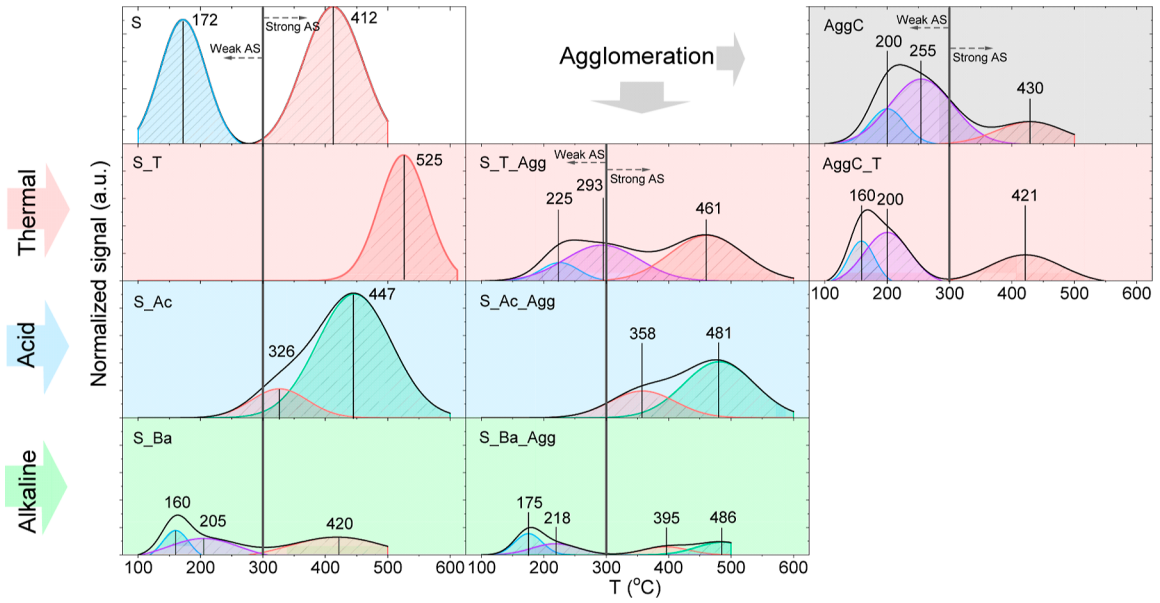

Figure 1. Acid site distribution of the samples.

acid site distribution, as shown in Table 3. In some samples (i.e., S_T_Agg), we observe a deviation bigger than 1.5 $mmol_{NH_3}·g^{-1}$, which could be related to some degree of ionic exchange between the three components of the agglomerated catalyst (mostly between zeolite and bentonite). The ionic exchange phenomenon is a common problem in agglomeration processes with some materials such as clays.[48−51]

Acidity is, with the micropore volume, the most important parameter in zeolite catalysts for MTO. The modified SAPO-34 samples have different acid strength and distribution (Figure 1) and micropore volume (Table 2). To account for that, we have defined the effective acid site concentration and density in Section 2.2. The values of these two parameters are shown in Table 4.

Table 4. Effective Acidity of the Samples

sample	effective acid site concentration C_{AS}* ($mmol_{NH_3}·g^{-1}$)	effective acid site density ρ_{AS}* ($mmolNH_3·cm^{-3}$)
S	11.9	31.3
AggC	18.0	100.2
S_T	14.4	50
S_T_Agg	11.3	65.5
AggC_T	9.9	111
S_Ac	20.1	57
S_Ac_Agg	10.0	58
S_Ba	7.4	248.1
S_Ba_Agg	4.9	153.1

From these calculations, it is worth noting that the effective acid site density of alkaline-treated samples is high because their micropore volume is low. As we show further on in this section (Figure 2), the alkaline treatment amorphizes the crystalline structure of the SAPO-34 and destroys its shape selectivity features. Because of that, it is mandatory to use these results carefully to explain the catalytic results or the coke formation.

The XRD patterns of the parent and modified samples (Figure 2a) and the agglomerated samples (Figure 2b) show

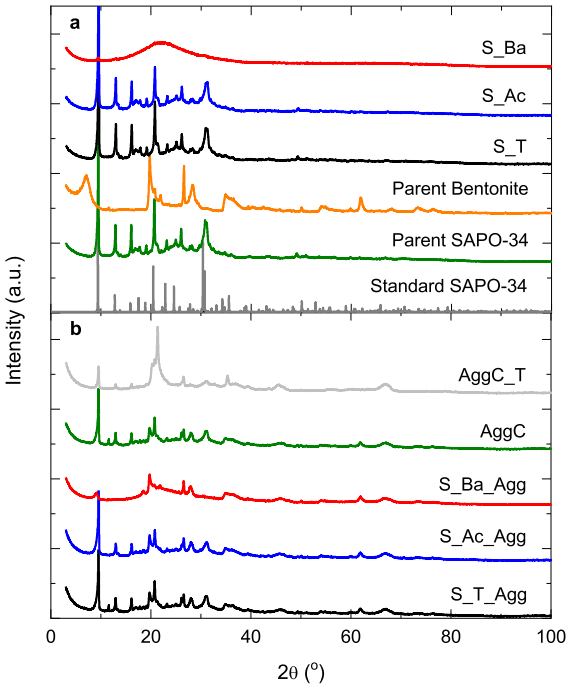

Figure 2. XRD patterns of the (a) standard, parent, and modified samples and (b) parent and modified agglomerated samples.

how the treatments applied to SAPO-34 modify its crystallinity. The parent sample shows some of the major peaks of the typical CHA structure,[52] which remain on all treated samples except the S_Ba.[41,47,52−55] In the latter, most of the zeolite crystallinity is destroyed, in agreement with the loss of micropore volume reported in Table 2.

The agglomerated samples (Figure 2b) show a pattern formed by the characteristic peaks of their three components: zeolite, bentonite, and alumina. In the parent agglomerated sample (AggC), all of the peaks from parent SAPO-34 could be found, in addition with those from the bentonite and alumina (with typical peaks at 38, 47, 61 and 68°). As the original framework on the thermally treated SAPO-34 sample

https://doi.org/10.1021/acs.iecr.3c03956
Ind. Eng. Chem. Res. XXXX, XXX, XXX−XXX

(S_T) is conserved, the agglomerated sample S_T_Agg displays a similar pattern. The same result could be applied to the acid-treated catalyst (S_Ac_Agg). The main difference is observed on the alkaline-treated S_Ba_Agg catalyst, which shows reduced intensities of the peaks corresponding to other compounds in the agglomerated sample because most of the zeolite was amorphized in the basic etching. Lastly, the parent catalyst subjected to the thermal treatment (AggC_T) has lost some of its crystallinity. Its XRD pattern lacks some of the peaks present in the original AggC catalyst probably because the difference in the thermal conductivity of its components favors the amorphization of part of its framework.

3.2. Catalytic Results. *3.2.1. Evolution of Conversion and Yields with TOS.* This section includes the results obtained from the catalytic tests of the agglomerated SAPO-34-based samples in a packed bed reactor, as well as the parent agglomerated catalyst (AggC) and the thermally treated parent catalyst (AggC_T). These include the evolution with time on stream (TOS) of conversion (of lumped MeOH and DME), olefin (C_2H_4 and C_3H_6) yield, and byproducts (CH_4 and CO) yield.

The evolution with TOS of the conversion of MeOH and DME for the parent and modified SAPO-34 catalysts is shown in Figure 3, where we observe a clear deactivation trend for

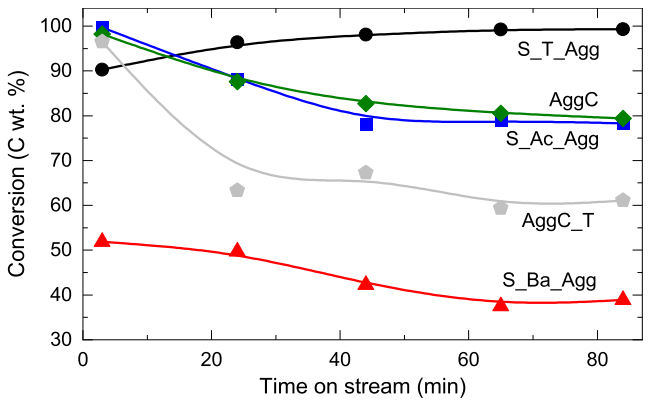

Figure 3. Conversion evolution with time on stream for the agglomerated SAPO-34 catalysts (see the lines for visual help).

most of the catalysts. For those that maintain the microporous structure, conversion is >90% at low TOS but steadily decreases over time. The conversion of AggC and S_Ac_Agg evolves similarly, dropping from 98 to 85 and 80%, respectively. This conversion drop occurs in 45 min, but after that it stabilizes. Conversion with the AggC_T originally is >95% but rapidly shrinks to below 65% after 25 min due to deactivation. This could relate to its low micropore volume, which blocks due to coke deposition before other catalysts. The conversion of S_T_Agg shows a different trend, starting at 90% and increasing up to close to 100% at 65 min. This evolution results from a shift in the reaction mechanism, which starts with the production of olefins and shifts to the CH_4 and CO production as the catalyst deactivates. This shift may be a slower competitive mechanism of methanol conversion that requires a high temperature (>450 °C) and the deactivation of the catalyst to be advanced, as shown in previous works and in additional experiments with SiC as catalyst.[8,40,56−58] This mechanism could be related to the presence of iron in the bentonite used for agglomeration.[56−59] Lastly, the S_Ba_Agg catalyst shows a low methanol conversion from the beginning of the reaction (around 50%), which further decreases upon catalyst deactivates. This could be an effect of the destruction of microporosity, the neutralization of most of the acid sites, or a combination of both during the alkaline treatment of the zeolite. The presence of a secondary mechanism is more noticeable in a packed bed configuration than in a fluidized bed because the catalyst deactivation profile follows a "cigar burn" model.[9,60,61] In other words, freshly fed methanol goes through the deactivated sections of the catalyst bed before reaching the fresh catalyst section, partially converting to produce CH_4 and CO along the way. Although the height of the catalyst bed (ca. 2 cm) could make this effect relevant, we consider that operating with a lower amount of catalyst would not provide enough sample mass to perform all characterization analyses.

Although the evolution of the conversion shows a clear trend with TOS, the evolution of product yields was not similar for all catalysts, as reported for light olefins (main products) and byproducts (CH_4 and CO) in Figure 4, respectively.

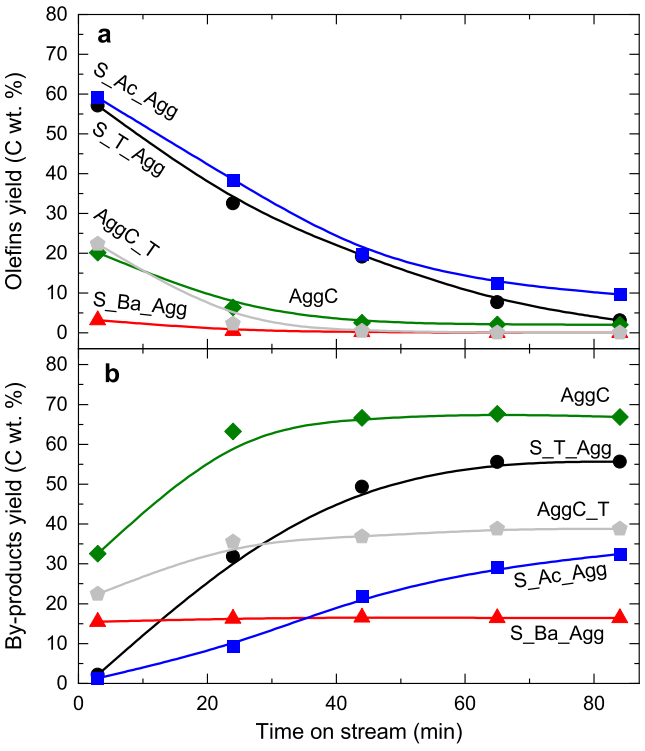

Figure 4. Olefin (a) and byproduct (b) yield evolution with time on stream for the SAPO-34 catalysts (lines for visual help).

Using the AggC sample, the yield of olefins decreases from 20 to <10% in 20 min (Figure 4a) due to rapid catalyst deactivation over the first minutes of reaction. Because of the coke formation and deposition, the catalyst quickly deactivates by suppressing the main reaction mechanism to produce olefins, and the secondary (and slower) mechanism for CH_4 and CO formation is promoted. The pore blockage has been identified as the main consequence of the coke formation as further analysis of coke has been revealed.[62−66] The results are similar for other catalysts (except S_Ba_Agg which deactivates by coke deposition over the acid sites) and will be discussed later in Section 3.3. The thermally treated AggC_T catalyst behaves similarly, providing an initial olefin yield >20% that drops <10% in 15 min.

https://doi.org/10.1021/acs.iecr.3c03956
Ind. Eng. Chem. Res. XXXX, XXX, XXX−XXX

The acid-treated S_Ac_Agg catalyst shows a better performance than AggC. The initial olefin yield not only is greater (60%) but also decreases slower (85 min to reach 10%). This may be an effect of its greater micropore volume, which allows a larger olefin production and deactivates at a slower rate, as a larger fraction of active sites remains available. In addition, this catalyst produces a lower byproduct yield through the whole reaction probably because the secondary mechanism had less relevance. At the beginning of the reaction, this catalyst has a yield of byproducts close to zero, which could suggest that the secondary mechanism may relate to a slower adsorption reaction in acid sites. We found a similar conclusion in previous works,[8,40,67] where the deactivated catalyst showed a high byproduct yield when the olefin yield was close to zero. This mechanism needs the combined effect of temperature and mild acidity in the catalyst, which acid peaks in TPD were missing in the fresh catalyst (Figure 1). Some authors suggest that coke species found in later stages of reaction (i.e., developed hydrocarbon chains) could provide this acidity.[68−71]

The S_T_Agg catalyst shows a deactivation trend similar to S_Ac_Agg. The olefin yield started near 60% and reached 10% at 60 min. The evolution of the thermal-treated sample, compared to that of S_Ac_Agg, could be the result of its different acid site concentrations, as both samples present a similar micropore volume (see Table 2). This S_T_Agg catalyst is suitable for the two previously mentioned reactions: the conversion of methanol into olefins and into CH_4 and CO, whose mechanisms are competitive. Moreover, the yield to main products shows a complete shift from 57% olefins to 56% byproducts (at the beginning and end of reaction TOS, respectively). This change in product distribution, and the fact that the conversion using the S_T_Agg catalyst is maintained at 90−100%, could indicate that the second mechanism somehow relates to the acidity of the coke species.

Lastly, the S_Ba_Agg catalyst provides the lowest olefin yield, below 5% through all of the reaction. Its byproduct yield is higher and stable (ca. 15%), which could be produced by its mild acidity in the larger pores. As stated before, the probable cause for deactivation on this catalyst is not the pore blockage but the acid site covering as this catalyst is predominantly macroporous.

These results clearly evidence that the micropore volume and the strength and distribution of acid sites play an important role in the performance of the catalysts as they behave differently in the production of olefins, byproducts, and coke. The initial distribution of olefin yield is shown in Figure S2 (Supporting Information). Figure 5a shows how the initial olefin yield correlates linearly with the effective acid site density (ρ_{AS}*) in such a way that the lower the effective acid site density is, the greater the initial olefin yield becomes. This result indicates that those catalysts with lower concentration and/or strength of acid sites and higher micropore volume have favored initial olefin yield, results that match with those found by other authors.[72,73] There are three main reasons for this effect. First, weaker acid sites facilitate the adsorption and desorption of hydrocarbons, allowing them to desorb easily before growing into larger molecules. Second, a lower concentration of these acid sites (by unit of catalyst mass) decreases the probability of bonding between hydrocarbon molecules adsorbed in different acid sites (bridging), and hence, they can preferentially desorb instead of producing a bulkier molecule. Lastly, larger micropore volumes decrease the degree of acid site clustering, which reduces the probability of bridge formation between adsorbed hydrocarbon molecules.[68,74,75]

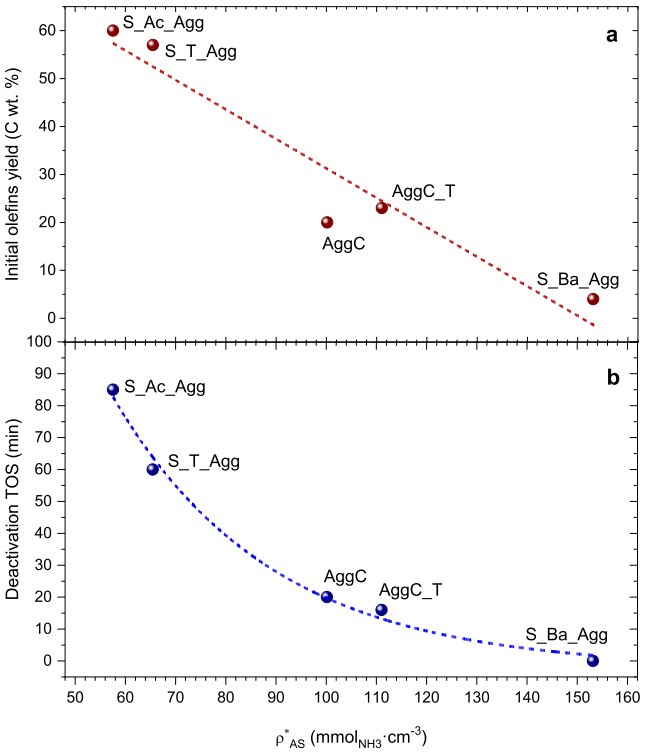

Figure 5. Initial olefin yield (a) and deactivation time (b) vs effective acid site density.

Furthermore, the effective acid site density also relates to the deactivation rate of the catalyst, as displayed in Figure 5b. The time that took the catalysts to deactivate (reach an olefin yield ≤10%) relates nonlinearly with the effective acid site density. The trend follows a power law probably caused by the inverse contribution of the micropore volume in ρ_{AS}*. Similar to the initial olefin yield, the deactivation time is greater for those catalysts with lower effective acid site density. This could be understood in two ways. On one hand, hydrocarbon molecules adsorb weakly over acid sites with lower strength, which results also in an easier desorption and subsequent diffusion of the products outside of the catalyst, resulting in a lower micropore blockage, which is the main reason for deactivation in small micropore zeolites such as SAPO-34. On the other hand, a lower effective acid site density, thus greater micropore volume, allows for a greater amount of coke deposition inside the catalyst structure before deactivation becomes relevant.

3.3. Coke Formation and Nature. *3.3.1. Overall Picture of Coke Formation.* The performance of catalysts in the MTO reaction relates closely to the formation and nature of the deactivating hydrocarbon species trapped within the catalyst structure, especially for those catalysts with higher diffusional restrictions caused by their microporosity. After reaction tests, the concentration of coke shows a clear increasing trend with the micropore volume (Figure 6). This nonlinear trend also shows the enhancing effect that the presence of interconnected SAPO-34 cavities has on coke trapping. A reasoning similar to the deactivation time applies for the trend of coke concentration with the micropore volume. It follows a potential trend probably to result from the three-dimensional features of the micropore volume. That is, a small increase in

https://doi.org/10.1021/acs.iecr.3c03956
Ind. Eng. Chem. Res. XXXX, XXX, XXX−XXX

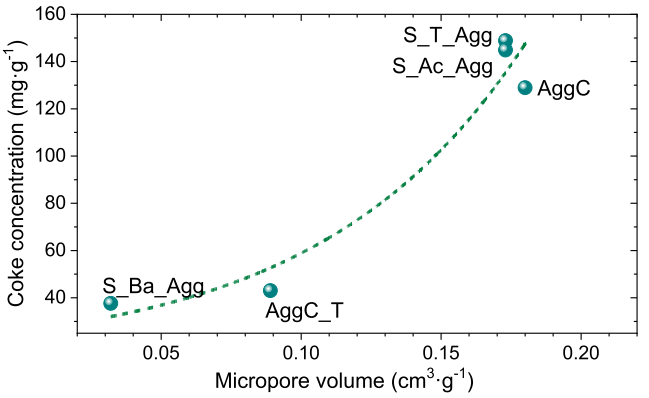

Figure 6. Final coke concentration vs micropore volume, $V_{\mu p}$.

micropore volume produces a big increase in the available space for coke buildup, especially at bigger volumes.

We classified the coke contained inside the catalyst structure following the criteria described in Section 2.3. In a previous work,[9] we proposed that volatile species are those hydrocarbon molecules that are active and able to desorb from acid sites. By this definition, we showed that they keep a constant concentration with TOS because once formed they desorb as products or grow to become non-volatile species. When volatile species desorb at advanced stages of the reaction, bigger molecules formed in the entrance of pores can block them. However, it is possible to identify these species by stripping at higher temperature than in the reaction when their diffusivity through blocked channels is improved. Non-volatile species originate from volatiles but are unable to desorb or exit through the small micropores of the zeolite structure. Even though they can be active, they accumulate and produce deactivation of the catalyst by the pore blockage. Figure 7 shows the final coke distribution and non-volatile coke density obtained from TPD/TPO analysis.

The profiles in Figure 7a show how the volatile species desorbed from the spent catalyst with their maximum desorbing rate at ca. 76 °C, with the exception of the S_Ba_Agg catalyst, whose profile is shifted toward higher temperatures with its maximum at 168 °C. This temperature displacement is related to the more aromatic and recalcitrant nature of the species deposited over the latter catalyst, where the secondary byproduct forming mechanism is dominant (see Figure 4b), with a minimal olefin production (Figure 4a). Moreover, the amount of volatile species deposited in the AggC_T and S_Ba_Agg catalysts per mass unit is significantly lower compared with the rest of the catalysts, which can be justified by their remarkably low specific surface and micropore volume (Table 2). Regarding the deactivating coke species in Figure 7b, very similar trends are observed in the TPO profiles, with maximum coke combustion rates at 517−547 °C for all the catalyst except S_Ba_Agg, with its maximum rate at 651 °C. The overall deposited coke on the S_T_Agg and S_Ac_Agg catalysts was analogue, showing that the textural properties have a greater impact on the coke formation with a little effect of the acidic properties. Conversely, the coke formed over the AggC and AggC_T catalysts was lower, following their microporosity trend (Table 2). In any case, in Figure 7c, we observe that for these catalysts the coke density (in milligrams of coke per catalyst micropore volume unit) is analogue, and the same occurs for the S_T_Agg and S_Ac_Agg catalysts. However, this value is clearly higher for

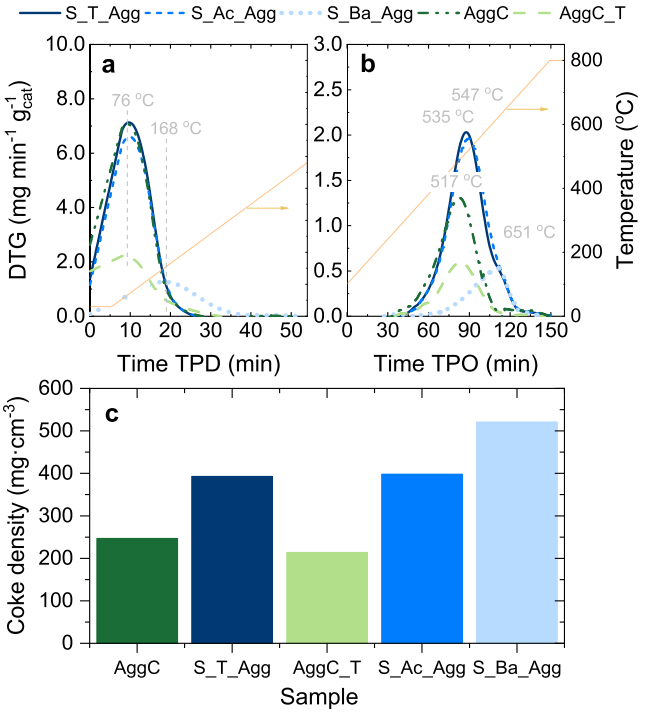

Figure 7. Final stripped (a) and burnt (b) coke and non-volatile coke density (c) obtained by TPD/TPO analysis.

the S_Ba_Agg catalyst, as its coke deposition is significant despite its very low microporosity. For this catalyst, it is worth noting that the alkaline treatment completely amorphized the structure of the zeolite (Figure 2) and reduced its micropore volume by 99.9% (from 0.38 to 0.03 $cm^3 \cdot g^{-1}$). This means that even having the smallest content of non-volatile coke (15.4 $mg \cdot g^{-1}$), S_Ba_Agg had the highest coke density (512 $mg \cdot cm^{-3}$) because its micropore volume is the lowest.

Our results suggest that as discussed in Figure 5a for the olefin yield, the acid site density is the determining factor conditioning coke deposition, which is confirmed by the results shown in Figure 8 displaying a linear trend between the acid site density and the density of non-volatile coke species.

Non-volatile coke density correlates inversely with effective acid site density. The greater the effective acid site density, the lower the density of non-volatile coke species. Although a lower density of these species could lead to lower deactivation, this could not be the case. At the end of reaction time, lower

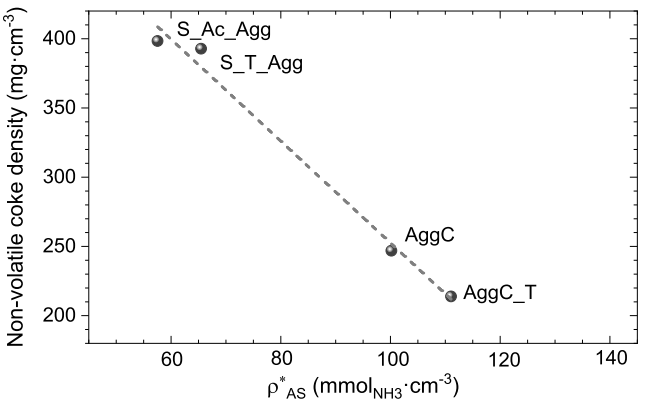

Figure 8. Final non-volatile coke density vs effective acid site density.

https://doi.org/10.1021/acs.iecr.3c03956
Ind. Eng. Chem. Res. XXXX, XXX, XXX−XXX

non-volatile coke density implies less clustered coke species; thus, the most probable scenario is that they formed close to micropore openings and block the access to the micropore structure. However, if non-volatile coke density is greater, these species probably formed in the cages and deactivation was slower as the majority of active sites remains accessible in the pores. This relates with effective acid site density, inversely with micropore volume, and directly with effective acid site concentration. On one hand, more micropore volume implies that there is a greater number of pore openings. Therefore, even though the catalyst suffers a certain pore blockage, still many pore openings remain available for reaction, as in the case of the S_T_Agg and S_Ac_Agg catalysts (Figures 3 and 5b). Moreover, this lower deactivation rate also plays in favor of higher olefin yields (Figure 5a). Nonetheless, the species formed in these two catalysts show a slightly more aromatic and condensed nature (with maximum combustion rates at 535−547 °C, see Figure 7b) compared to their AggC and AggC_T counterparts (517 °C), as a higher effective acid site concentration involves more and/or stronger acid sites, which could explain harmed desorption of bonded hydrocarbons, easier growth of chains, and faster blockage of pore openings and deactivation.

Non-volatile coke species relate directly with the initial olefin yield (Figure 9a) and the deactivation time (Figure 9b).

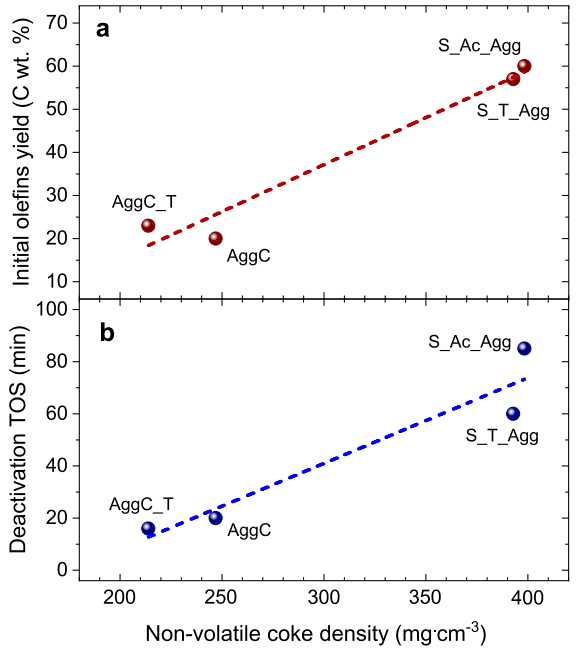

Figure 9. Initial olefin yield (a) and deactivation time (b) vs non-volatile coke density at the end of experiments.

In MTO with small pores zeolites such as SAPO-34, the main reason for deactivation is the pore blockage, which is caused by the growth of coke species up to the point where they are not able to abandon the micropore structure. These non-volatile species can form clusters or grow dispersed through the whole structure of the zeolite. In the first case, these species could form in the cages of the zeolite, growing larger but allowing diffusion of reactives and molecules through the rest of channels. In the second case, it is probable that they block the access to the structure because it is the first point of fresh methanol arrival. Taking this into account, a higher density of non-volatile coke would be preferable because it slows down deactivation. The relation between olefin yield and non-volatile coke density follows a similar logic. Clustered species formed in cages tend to grow more, which makes them more susceptible to cracking reactions,[76] thus producing more olefins. This is especially relevant because ethylene, one of the main products, forms through the aromatics cycle in the dual cycle mechanism.[77,78]

3.3.2. Soluble Coke. The nature of the soluble coke accumulated in the zeolite at the end of the catalytic tests is a key result. We analyzed it by ^{1}H NMR and quantified the hydrogen bonded to aliphatic (paraffinic or naphthenic) and aromatic (mono- or polyaromatic) coke species through the integration of the obtained spectra. It is worthy to note that ^{1}H NMR does not quantify the type of coke species contained in the catalyst but the contribution of hydrogen bonds in those species. This means that an H^+ in an aliphatic structure could also bind to an aromatic ring, as shown in Figure S3 (Supporting Information). From this quantification, we detected the correlation between the aliphatic and aromatic hydrogen with the acid site density, as plotted in Figure 10.

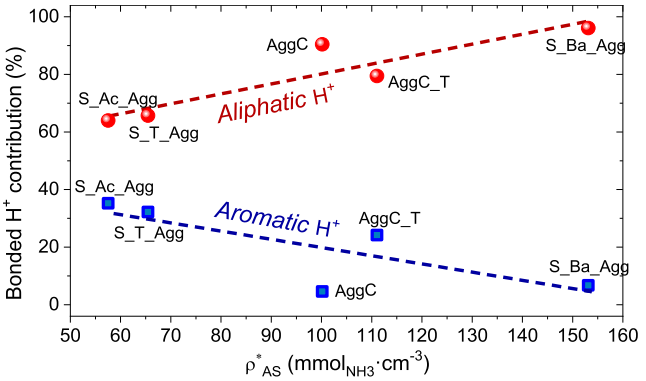

Figure 10. Proton species distribution in the soluble coke vs the effective acid site density.

The observed results are in line with those in Figure 7b which point at the formation of an overall more dehydrogenated, hence condensed/aromatic, type of coke with the S_T_Agg and S_Ac_Agg catalysts, which have a lower acid site density compared to the coke formed over the AggC and AggC_T samples. This indicates that both a higher amount and/or stronger acid sites partially prevent coke species from evolving into bulkier compounds. Conversely, the soluble coke formed using the S_Ba_Agg catalyst presents the lowest aromaticity degree, which, in combination with the microporous nature of this catalyst, indicates that coke species grow in a more "disorganized" fashion on this catalyst and without steric limitations.

It is relevant to note that, in a pool of hydrocarbon molecules, the contribution of the aliphatic H^+ is usually greater than that of the aromatic H^+. As an example of this, the amount of paraffinic hydrogen in hexane is greater than those of naphthenic H^+ in cyclohexane and aromatic H^+ in benzene, and thus, H^+ contribution is usually greater (Figure S4, Supporting Information).

Figure 11a displays the dependence of paraffinic and naphthenic H^+ on the acid site concentration of the catalysts. The results evidence that a higher acid site concentration (implying either more acid sites or stronger ones) favors the

https://doi.org/10.1021/acs.iecr.3c03956
Ind. Eng. Chem. Res. XXXX, XXX, XXX−XXX

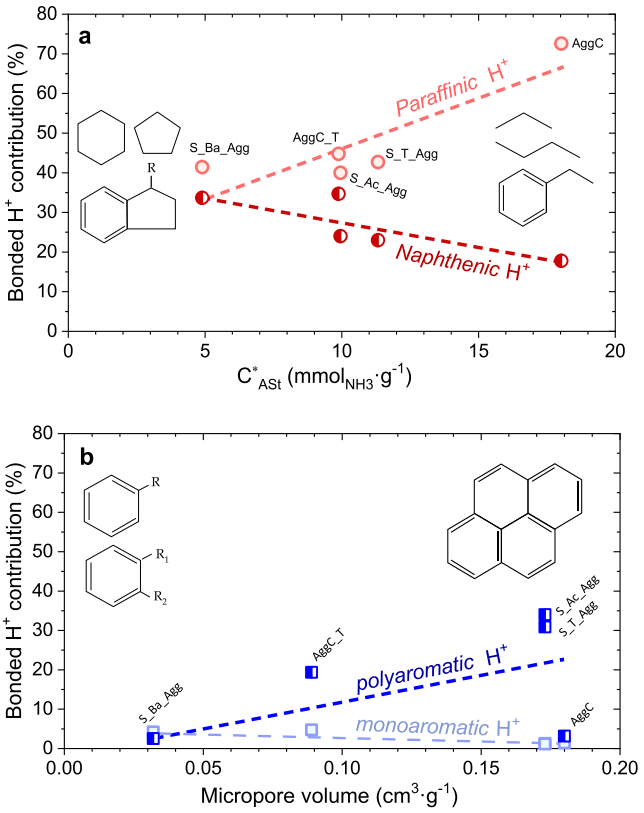

Figure 11. H^+ distribution of proton species in coke for (a) the aliphatic vs effective acid site concentration and (b) the aromatic vs micropore volume.

formation of either aliphatic coke species or smaller aromatic species with a higher aliphatic branching degree as ring-opening reactions and hydrogen transfer are enhanced. This seems coherent, as aliphatic species are comparatively smaller than aromatic species, and their formation and conversion are less restricted by the porous properties of the catalyst and depend primarily on their acid features. Conversely, the growth of (poly-)aromatics is dominated by the microporosity of the catalyst, as shown in Figure 11b. The increase in hydrogen bonded to polyaromatics with the micropore volume could partially relate to a cross-cage linkage between species formed in the cages of the zeolite,[15,74,79] as a higher micropore volume increases the probability of cross-cage bridging. The shape selectivity of the cavities of the SAPO-34 zeolite determines the more ordered growth of polyaromatics within these cages, showing a dominant effect over the growth of these unsaturated species with a little effect of the acid features of the catalyst.

As a general trend, Figure 12 schematically captures the dependence of the nature (paraffinic, naphthenic, and aromatic) of the formed coke species on the acidic and structural properties of the agglomerated SAPO-34-based catalysts. When the coke species (or coke precursors) are mono- or bicyclic compounds, their growth is little conditioned by the pore structure, and the acid site concentration will predominantly determine their saturation degree and the extent of the aliphatic branching of these molecules, which is boosted by a higher acid site concentration. However, when these coke species remain trapped within the zeolite cavities, their enlargement is determined by the shape selectivity of the SAPO-34 zeolite, with the

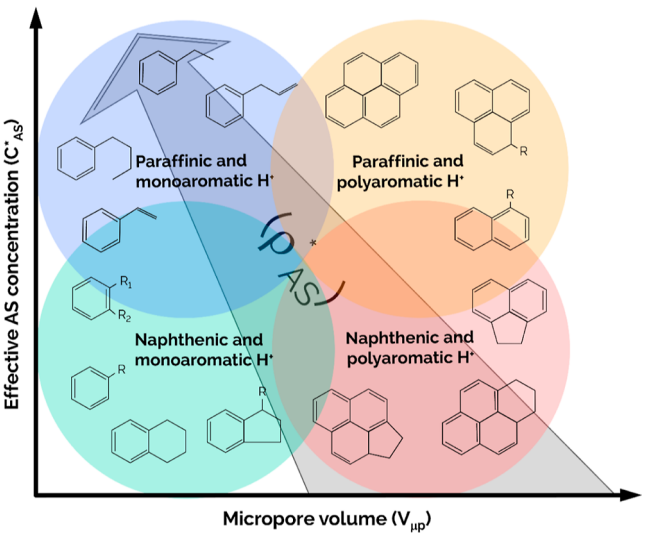

Figure 12. Proposed dependence of the type of coke species (paraffinic, naphthenic, or aromatic) formed on the acidity and structural properties of agglomerated SAPO-34-based catalysts.

possibility of forming bridged aromatic clusters which are located within adjacent zeolite cavities and cannot further grow within this void. All in all, our results demonstrate that the modification of the catalyst properties (namely, acid site concentration and micropore volume) through acid or thermal treatments will have a "tuning" effect on the nature of coke formed on the catalyst. This coke, as responsible of deactivation, relates to active time and olefin yield, which can improve by reducing the effective acid site density.

4. CONCLUSIONS

Modifying zeolites by post-treatment methods is a common way to tune their properties for specific purposes. Some of the treatments applied in this work produced samples with different properties that behaved differently in catalytic tests.

Thermal treatment reduced the micropore volume and the total acidity of SAPO-34 by a partial collapse of its structure and a combined effect of dehydroxylation and dehydration. These effects produced the disappearance of weak acid sites, increasing the effective acid site density by 60%. The same treatment applied over the previously agglomerated catalyst produced a loss of half its micropore volume and a third of its weak and strong acidity, resulting in an effective acid site density 10% greater. This was probably because the sample was a physical mixture of components that heats in a different way during the heating step of the treatment.

Chemical treatments also modified the zeolite. On one hand, the acid treatment resulted in a zeolite with a slightly reduced micropore volume and total acidity but similar crystallinity. In addition to selective etching of some Al and P from its structure, its acid site distribution also changed. Acid treatment produced the disappearance of weak acid sites and the formation of new strong acid sites, probably caused by the generation of bridging OH^- groups. This doubled the effective acid site concentration and increased the effective acid site density by 80%. On the other hand, the basic treatment completely amorphized the framework of the zeolite, transformed micropores into macropores, reduced the weak and strong acidity, and etched P and Al.

https://doi.org/10.1021/acs.iecr.3c03956
Ind. Eng. Chem. Res. XXXX, XXX, XXX−XXX

After agglomeration, the properties of modified SAPO-34 catalysts were the result of a weighted mean of those from their components. However, there were some discrepancies in acidity, probably caused by phenomena related to ionic exchange with bentonite. Catalytic tests showed that the best catalysts, regarding olefin production, were those obtained from thermal and acid modification of SAPO-34, which showed a similar performance and a deactivation time 300 and 425% greater compared to the parent catalyst, respectively. For all catalysts, we found a relation between both initial olefin yield and deactivation time with effective acid site density. The first one followed an inversely linear trend, while the second one showed an inversely power trend, which suggested that the formation of olefins depends on the nature, amount, and distribution of acid sites, while deactivation relates to olefins and other hydrocarbon formation. To corroborate that we classify the nature of bonded hydrogen in soluble coke by H^+ NMR, which showed that those samples with lower effective acid site density produced coke with more naphthenic and monoaromatic H^+. This can relate to slower deactivation and the formation of light olefins through dealkylation and cracking reactions, a hypothesis that agrees with the dual cycle mechanism.

Because the conversion of methanol to light olefins is an acid site-driven reaction, when comparing catalysts with different properties, it is necessary to define new parameters that account for the strength, concentration, and distribution of acid sites. In order to do that, we defined the effective acid site concentration (C_{AS}*) and density (ρ_{AS}*) to represent how strong, numerous, and volume dispersed those acid sites are in the three-dimensional microporous structure of the catalysts. These parameters can help to correlate acid strength, density, and micropore volume with conversion, yield, and deactivation.

■ ASSOCIATED CONTENT

Supporting Information

The Supporting Information is available free of charge at https://pubs.acs.org/doi/10.1021/acs.iecr.3c03956.

Micropore size distribution of SAPO-34-based samples, initial distribution of olefin yield (ethylene and propylene), schematic representation of proton NMR species classification, and H^+ contribution of C_6 hydrocarbons (PDF)

■ AUTHOR INFORMATION

Corresponding Author

Javier Herguido − *Catalysis and Reaction Engineering Group (CREG), Department of Chemical and Environmental Engineering, Aragon Institute of Engineering Research (I3A), Universidad Zaragoza, Zaragoza 50018, Spain;* orcid.org/0000-0003-1940-9597; Email: jhergui@unizar.es

Authors

Diego Zapater − *Catalysis and Reaction Engineering Group (CREG), Department of Chemical and Environmental Engineering, Aragon Institute of Engineering Research (I3A), Universidad Zaragoza, Zaragoza 50018, Spain; Multiscale Reaction Engineering, KAUST Catalysis Center, King Abdullah University of Science and Technology (KAUST), Thuwal 23955-6900, Saudi Arabia*

Javier Lasobras − *Catalysis and Reaction Engineering Group (CREG), Department of Chemical and Environmental Engineering, Aragon Institute of Engineering Research (I3A), Universidad Zaragoza, Zaragoza 50018, Spain;* orcid.org/0000-0002-7488-6196

Naydu Zambrano − *Multiscale Reaction Engineering, KAUST Catalysis Center, King Abdullah University of Science and Technology (KAUST), Thuwal 23955-6900, Saudi Arabia*

Idoia Hita − *Multiscale Reaction Engineering, KAUST Catalysis Center, King Abdullah University of Science and Technology (KAUST), Thuwal 23955-6900, Saudi Arabia*

Pedro Castaño − *Multiscale Reaction Engineering, KAUST Catalysis Center, King Abdullah University of Science and Technology (KAUST), Thuwal 23955-6900, Saudi Arabia;* orcid.org/0000-0002-6454-9321

Jaime Soler − *Catalysis and Reaction Engineering Group (CREG), Department of Chemical and Environmental Engineering, Aragon Institute of Engineering Research (I3A), Universidad Zaragoza, Zaragoza 50018, Spain;* orcid.org/0000-0001-9022-2835

Miguel Menéndez − *Catalysis and Reaction Engineering Group (CREG), Department of Chemical and Environmental Engineering, Aragon Institute of Engineering Research (I3A), Universidad Zaragoza, Zaragoza 50018, Spain;* orcid.org/0000-0002-2494-102X

Complete contact information is available at: https://pubs.acs.org/10.1021/acs.iecr.3c03956

Notes

The authors declare no competing financial interest.

■ ACKNOWLEDGMENTS

Authors acknowledge grant CTQ2016-76533-R funded by MCIN/AEI/10.13039/501100011033. D. Zapater acknowledges grant BES-2017-082052 funded by MCIN/AEI/10.13039/501100011033.

■ ABBREVIATIONS

MTO	methanol to olefins
ZSM	zeolite socony mobil
SAPO	silico-alumino-phosphate oxide
HSAPO	silico-alumino-phosphate oxide in its acid form
CHA	chabazite
S	raw SAPO-34 sample
B	raw bentonite sample
AggC	agglomerated catalyst
S_T	SAPO-34 sample after the thermal treatment
S_T_Agg	agglomerated SAPO-34 sample after the thermal treatment
AggC_T	agglomerated catalyst after the thermal treatment
S_Ac	SAPO-34 sample after the acid treatment
S_Ac_Agg	agglomerated SAPO-34 sample after the acid treatment
S_Ba	SAPO-34 sample after the alkaline treatment
S_Ba_Agg	agglomerated SAPO-34 sample after the alkaline treatment
XRF	X-ray fluorescence
XRD	X-ray diffraction
TPD	temperature-programed desorption
m/z	mass-to-charge ratio
ASw	weak acid sites
ASs	strong acid sites

https://doi.org/10.1021/acs.iecr.3c03956
Ind. Eng. Chem. Res. XXXX, XXX, XXX−XXX

GC−MS	gas chromatography−mass spectroscopy
NMR	^{1}H nuclear magnetic resonance
TG	thermogravimetry
TPO	temperature-programed oxidation
TGA	thermogravimetric analysis

PARAMETERS

C_{AS}* effective acid site concentration, $mmol_{NH_3}\cdot g^{-1}$
ρ_{AS}* effective acid site density, $mmol_{NH_3}\cdot cm^{-3}$
$V_{\mu p}$ micropore volume, $cm^3\cdot g^{-1}$
dp particle diameter, μm
T_i desorption temperature of the (weak) peak i, °C
T_j desorption temperature of the (strong) peak j, °C
$\frac{A_i}{A_{weak}}$ area of peak i over the total area of weak acid sites, dimensionless
$\frac{A_j}{A_{strong}}$ area of peak j over the total area of strong acid sites, dimensionless
W/F_{MeOH} catalyst weight to methanol molar flow ratio, $g\cdot h\cdot mol^{-1}$
gC_k mass of carbon from the component k, g
X_k conversion of the component k (in carbon mass basis), C wt %
Y_i yield to product i (in carbon mass basis), C wt %

REFERENCES

(1) Chen, D.; Moljord, K.; Holmen, A. A Methanol to Olefins Review: Diffusion, Coke Formation and Deactivation on SAPO Type Catalysts. *Microporous Mesoporous Mater.* **2012**, *164*, 239−250.
(2) Ahmadova, R. H.; Ibrahimov, H. J.; Babayeva, F. A.; Rustamov, M. I.; Kondratenko, E. V. The Perspective of Methanol to Olefins Process over Nanostructured Zeolite Catalysts, Mechanism and Synthesized Methods: A Review. *Processes Petrochem. Oil Refin.* **2017**, *18* (2), 171−187.
(3) Yu, J.; Xu, R. Rich Structure Chemistry in the Aluminophosphate Family. *Acc. Chem. Res.* **2003**, *36* (7), 481−490.
(4) Corma, A. From Microporous to Mesoporous Molecular Sieve Materials and their Use in Catalysis. *Chem. Rev.* **1997**, *97* (6), 2373−2420.
(5) Lefevere, J.; Mullens, S.; Meynen, V.; Noyen, J. Structured Catalysts for Methanol-to-Olefins Conversion: A Review. *Chem. Pap.* **2014**, *68* (9), 1143−1153.
(6) Yang, L.; Wang, C.; Zhang, L.; Dai, W.; Chu, Y.; Xu, J.; Wu, G.; Gao, M.; Liu, W.; Xu, Z.; Wang, P.; Guan, N.; Dyballa, M.; Ye, M.; Deng, F.; Fan, W.; Li, L. Stabilizing the Framework of SAPO-34 Zeolite toward Long-Term Methanol-to-Olefins Conversion. *Nat. Commun.* **2021**, *12* (1), 4661−4671.
(7) Wu, L.; Hensen, E. J. M. Comparison of Mesoporous SSZ-13 and SAPO-34 Zeolite Catalysts for the Methanol-to-Olefins Reaction. *Catal. Today* **2014**, *235*, 160−168.
(8) Zapater, D.; Lasobras, J.; Soler, J.; Herguido, J.; Menéndez, M. Counteracting SAPO-34 Catalyst Deactivation in MTO Process Using a Two Zone Fluidized Bed Reactor: Reactor Testing and Process Viability. *Catal. Today* **2021**, *362*, 155−161.
(9) Zapater, D.; Lasobras, J.; Soler, J.; Herguido, J.; Menéndez, M. MTO with SAPO-34 in a Fixed-Bed Reactor: Deactivation Profiles. *Ind. Eng. Chem. Res.* **2021**, *60* (45), 16162−16170.
(10) Valecillos, J.; Epelde, E.; Albo, J.; Aguayo, A. T.; Bilbao, J.; Castaño, P. Slowing down the Deactivation of H-ZSM-5 Zeolite Catalyst in the Methanol-to-Olefin (MTO) Reaction by P or Zn Modifications. *Catal. Today* **2020**, *348*, 243−256.
(11) Sanz-Martínez, A.; Lasobras, J.; Soler, J.; Herguido, J.; Menéndez, M. Methanol to Gasoline (MTG): Parametric Study and Validation of the Process in a Two-Zone Fluidized Bed Reactor (TZFBR). *J. Ind. Eng. Chem.* **2022**, *113*, 189−195.
(12) Lasobras, J.; Medrano, J. A.; Soler, J.; Herguido, J.; Menéndez, M.; Jimenez, A.; Da Silva, M.; Franco, M. J.; Barrio, I.; Lázaro, J. Preparation of Mo/HZSM-5/Bentonite Catalyst for Methane Aromatization in a Fluidized Bed Reactor. *Int. J. Chem. React. Eng.* **2017**, *15* (5), 20170081.
(13) Gayubo, A. G.; Aguayo, A. T.; Sánchez del Campo, A. E.; Tarrío, A. M.; Bilbao, J. Kinetic Modeling of Methanol Transformation into Olefins on a SAPO-34 Catalyst. *Ind. Eng. Chem. Res.* **2000**, *39* (2), 292−300.
(14) Rojo-Gama, D.; Mentel, L.; Kalantzopoulos, G. N.; Pappas, D. K.; Dovgaliuk, I.; Olsbye, U.; Lillerud, K. P.; Beato, P.; Lundegaard, L. F.; Wragg, D. S.; Svelle, S. Deactivation of Zeolite Catalyst H-ZSM-5 during Conversion of Methanol to Gasoline: Operando Time- and Space-Resolved X-Ray Diffraction. *J. Phys. Chem. Lett.* **2018**, *9* (6), 1324−1328.
(15) Luo, M.; Fu, Y.; Hu, B.; Wang, D.; Wang, B.; Mao, G. Water Inhibits the Conversion and Coking of Olefins on SAPO-34. *Appl. Catal., A* **2019**, *570*, 209−217.
(16) Nieskens, D. L. S.; Lunn, J. D.; Malek, A. Understanding the Enhanced Lifetime of SAPO-34 in a Direct Syngas-to-Hydrocarbons Process. *ACS Catal.* **2019**, *9* (1), 691−700.
(17) Dai, W.; Wu, G.; Li, L.; Guan, N.; Hunger, M. Mechanisms of the Deactivation of SAPO-34 Materials with Different Crystal Sizes Applied as MTO Catalysts. *ACS Catal.* **2013**, *3* (4), 588−596.
(18) Rojo-Gama, D.; Signorile, M.; Bonino, F.; Bordiga, S.; Olsbye, U.; Lillerud, K. P.; Beato, P.; Svelle, S. Structure-Deactivation Relationships in Zeolites during the Methanol-to-Hydrocarbons Reaction: Complementary Assessments of the Coke Content. *J. Catal.* **2017**, *351*, 33−48.
(19) Gao, S.; Xu, S.; Wei, Y.; Qiao, Q.; Xu, Z.; Wu, X.; Zhang, M.; He, Y.; Xu, S.; Liu, Z. Insight into the Deactivation Mode of Methanol-to-Olefins Conversion over SAPO-34: Coke, Diffusion, and Acidic Site Accessibility. *J. Catal.* **2018**, *367*, 306−314.
(20) Hita, I.; Mohamed, H. O.; Attada, Y.; Zambrano, N.; Zhang, W.; Ramírez, A.; Castaño, P. Direct Analysis at Temporal and Molecular Level of Deactivating Coke Species Formed on Zeolite Catalysts with Diverse Pore Topologies. *Catal. Sci. Technol.* **2023**, *13* (5), 1288−1300.
(21) Borodina, E.; Sharbini Harun Kamaluddin, H.; Meirer, F.; Mokhtar, M.; Asiri, A. M.; Al-Thabaiti, S. A.; Basahel, S. N.; Ruiz-Martinez, J.; Weckhuysen, B. M. Influence of the Reaction Temperature on the Nature of the Active and Deactivating Species during Methanol-to-Olefins Conversion over H-SAPO-34. *ACS Catal.* **2017**, *7* (8), 5268−5281.
(22) Zhou, J.; Zhi, Y.; Zhang, J.; Liu, Z.; Zhang, T.; He, Y.; Zheng, A.; Ye, M.; Wei, Y.; Liu, Z. Presituated "Coke"-Determined Mechanistic Route for Ethene Formation in the Methanol-to-Olefins Process on SAPO-34 Catalyst. *J. Catal.* **2019**, *377*, 153−162.
(23) Ghavipour, M.; Behbahani, R. M.; Moradi, G. R.; Soleimanimehr, A. Methanol Dehydration over Alkali-Modified H-ZSM-5; Effect of Temperature and Water Dilution on Products Distribution. *Fuel* **2013**, *113*, 310−317.
(24) De Wispelaere, K.; Wondergem, C. S.; Ensing, B.; Hemelsoet, K.; Meijer, E. J.; Weckhuysen, B. M.; Van Speybroeck, V.; Ruiz-Martínez, J. Insight into the Effect of Water on the Methanol-to-Olefins Conversion in H-SAPO-34 from Molecular Simulations and in Situ Microspectroscopy. *ACS Catal.* **2016**, *6* (3), 1991−2002.
(25) Sun, Q.; Xie, Z.; Yu, J. The State-of-the-Art Synthetic Strategies for SAPO-34 Zeolite Catalysts in Methanol-to-Olefin Conversion. *Natl. Sci. Rev.* **2018**, *5* (4), 542−558.
(26) Verboekend, D.; Milina, M.; Pérez-Ramírez, J. Hierarchical Silicoaluminophosphates by Postsynthetic Modification: Influence of Topology, Composition, and Silicon Distribution. *Chem. Mater.* **2014**, *26* (15), 4552−4562.
(27) Valtchev, V.; Majano, G.; Mintova, S.; Pérez-Ramírez, J. Tailored Crystalline Microporous Materials by Post-Synthesis Modification. *Chem. Soc. Rev.* **2013**, *42* (1), 263−290.
(28) Aramburo, L. R.; Ruiz-Martínez, J.; Sommer, L.; Arstad, B.; Buitrago-Sierra, R.; Sepúlveda-Escribano, A.; Zandbergen, H. W.;

https://doi.org/10.1021/acs.iecr.3c03956
Ind. Eng. Chem. Res. XXXX, XXX, XXX−XXX

Olsbye, U.; de Groot, F. M. F.; Weckhuysen, B. M. X-Ray Imaging of SAPO-34 Molecular Sieves at the Nanoscale: Influence of Steaming on the Methanol-to-Hydrocarbons Reaction. *ChemCatChem* **2013**, *5* (6), 1386−1394.
(29) Guan, X.; Zhang, F.; Wu, G.; Guan, N. Synthesis and Characterization of a Basic Molecular Sieve: Nitrogen-Incorporated SAPO-34. *Mater. Lett.* **2006**, *60* (25−26), 3141−3144.
(30) Buchholz, A.; Wang, W.; Xu, M.; Arnold, A.; Hunger, M. Thermal stability and dehydroxylation of Brønsted acid sites in silicoaluminophosphates H-SAPO-11, H-SAPO-18, H-SAPO-31, and H-SAPO-34 investigated by multi-nuclear solid-state NMR spectroscopy. *Microporous Mesoporous Mater.* **2002**, *56* (3), 267−278.
(31) Choi, K. H.; Lee, D. H.; Kim, H. S.; Park, C. S.; Kim, Y. H. Effects of Acid Treatment of SAPO-34 on the Catalytic Lifetime and Light Olefin Selectivity during DTO Reaction. *Appl. Chem. Eng.* **2015**, *26* (2), 217−223.
(32) Yang, G.; Han, J.; Huang, Y.; Chen, X.; Valtchev, V. Busting the Efficiency of SAPO-34 Catalysts for the Methanol-to-Olefin Conversion by Post-Synthesis Methods. *Chin. J. Chem. Eng.* **2020**, *28* (8), 2022−2027.
(33) Qiao, Y.; Yang, M.; Gao, B.; Wang, L.; Tian, P.; Xu, S.; Liu, Z. Creation of Hollow SAPO-34 Single Crystals: Via Alkaline or Acid Etching. *Chem. Commun.* **2016**, *52* (33), 5718−5721.
(34) Gimeno, M. P.; Soler, J.; Herguido, J.; Menéndez, M. Use of Fluidized Bed Reactors for Direct Gas Phase Oxidation of Benzene to Phenol. *Ind. Eng. Chem. Res.* **2010**, *49* (15), 6810−6814.
(35) Gimeno, M. P.; Soler, J.; Herguido, J.; Menéndez, M. Counteracting Catalyst Deactivation in Methane Aromatization with a Two Zone Fluidized Bed Reactor. *Ind. Eng. Chem. Res.* **2010**, *49* (3), 996−1000.
(36) Lachén, J.; Durán, P.; Menéndez, M.; Peña, J.; Herguido, J. Biogas to High Purity Hydrogen by Methane Dry Reforming in TZFBR+MB and Exhaustion by Steam-Iron Process. Techno-Economic Assessment. *Int. J. Hydrogen Energy* **2018**, *43* (26), 11663−11675.
(37) Ugarte, P.; Durán, P.; Lasobras, J.; Soler, J.; Menéndez, M.; Herguido, J. Dry Reforming of Biogas in Fluidized Bed: Process Intensification. *Int. J. Hydrogen Energy* **2017**, *42* (19), 13589−13597.
(38) Tschernich, R. *Zeolites of the World*; Geoscience Press, Inc.: Phoenix, AZ, 1992.
(39) Cruciani, G. Zeolites upon Heating: Factors Governing Their Thermal Stability and Structural Changes. *J. Phys. Chem. Solids* **2006**, *67* (9−10), 1973−1994.
(40) Zapater, D.; Lasobras, J.; Soler, J.; Herguido, J.; Menéndez, M. Temperature and Dilution Effects on MTO Process with a SAPO-34-Based Catalyst in Fluidized Bed Reactor. *Catal. Today* **2022**, *394*−*396*, 219−224.
(41) Shen, W.; Li, X.; Wei, Y.; Tian, P.; Deng, F.; Han, X.; Bao, X. A Study of the Acidity of SAPO-34 by Solid-State NMR Spectroscopy. *Microporous Mesoporous Mater.* **2012**, *158*, 19−25.
(42) Król, M. K.; Jeleń, P. The Effect of Heat Treatment on the Structure of Zeolite A. *Materials* **2021**, *14* (16), 4642.
(43) Cadar, O.; Senila, M.; Hoaghia, M. A.; Scurtu, D.; Miu, I.; Levei, E. A. Effects of Thermal Treatment on Natural Clinoptilolite-Rich Zeolite Behavior in Simulated Biological Fluids. *Molecules* **2020**, *25* (11), 2570.
(44) Combariza, A. F.; Sastre, G.; Corma, A. Propane/Propylene Diffusion in Zeolites: Framework Dynamics. *J. Phys. Chem. C* **2009**, *113* (26), 11246−11253.
(45) Watanabe, Y.; Koiwai, A.; Takeuchi, H.; Hyodo, S. A.; Noda, S. Multinuclear NMR Studies on the Thermal Stability of SAPO-34. *J. Catal.* **1993**, *143* (2), 430−436.
(46) Ates, A.; Hardacre, C. The Effect of Various Treatment Conditions on Natural Zeolites: Ion Exchange, Acidic, Thermal and Steam Treatments. *J. Colloid Interface Sci.* **2012**, *372* (1), 130−140.
(47) Ren, S.; Liu, G.; Wu, X.; Chen, X.; Wu, M.; Zeng, G.; Liu, Z.; Sun, Y. Enhanced MTO Performance over Acid Treated Hierarchical SAPO-34. *Chin. J. Catal.* **2017**, *38* (1), 123−130.
(48) Dorado, F.; Romero, R.; Cañizares, P. Influence of Clay Binders on the Performance of Pd/HZSM-5 Catalysts for the Hydroisomerization of n-Butane. *Ind. Eng. Chem. Res.* **2001**, *40* (16), 3428−3434.
(49) Cobzaru, C.; Inglezakis; Chapter, V. Ion Exchange. *Progress in Filtration and Separation*; Elsevier Ltd, 2015; pp 425−498.
(50) Li, Y. Y.; Perera, S. P.; Crittenden, B. D.; Bridgwater, J. The Effect of the Binder on the Manufacture of a 5A Zeolite Monolith. *Powder Technol.* **2001**, *116*, 85−96.
(51) Holtzer, M.; Bobrowski, A.; Żymankowska-Kumon, S. Temperature Influence on Structural Changes of Foundry Bentonites. *J. Mol. Struct.* **2011**, *1004* (1−3), 102−108.
(52) IZA Structure Commission. XRD powder pattern of Chabazite. https://europe.iza-structure.org/IZA-SC/pow_pat.php?STC=CHA&ID=CHA_0 (accessed Oct 29, 2023).
(53) Kong, C.; Zhu, J.; Liu, S.; Wang, Y. SAPO-34 with a Low Acidity Outer Layer by Epitaxial Growth and Its Improved MTO Performance. *RSC Adv.* **2017**, *7* (63), 39889−39898.
(54) Cao, Y.; Shen, T.; Guo, W.; Song, X.; Kong, L.; Wang, L. Application of F- Modified Fe-SAPO-34 as a New Photo-Catalyst in Printing and Dyeing Wastewater Treatment. *IOP Conf. Ser.: Mater. Sci. Eng.* **2020**, *729*, 012057.
(55) Vistad, B.; Akporiaye, D. E.; Lillerud, K. P. Identification of a Key Precursor Phase for Synthesis of SAPO-34 and Kinetics of Formation Investigated by in Situ X-Ray Diffraction. *J. Phys. Chem. B* **2001**, *105* (50), 12437−12447.
(56) Schulz, H. Coking" of Zeolites during Methanol Conversion: Basic Reactions of the MTO-MTP- and MTG Processes. *Catal. Today* **2010**, *154* (3−4), 183−194.
(57) Wu, X.; Abraha, M. G.; Anthony, R. G. Methanol Conversion on SAPO-34: Reaction Condition for Fixed-Bed Reactor. *Appl. Catal., A* **2004**, *260* (1), 63−69.
(58) Obrzut, D. L.; Adekkanattu, P. M.; Thundimadathil, J.; Liu, J.; Dubois, D. R.; Guin, J. A. Reducing Methane Formation in Methanol to Olefins Reaction on Metal Impregnated SAPO-34 Molecular Sieve. *React. Kinet. Catal. Lett.* **2003**, *80* (1), 113−121.
(59) Ozbek, M. O.; Niemantsverdriet, J. H. Methane, Formaldehyde and Methanol Formation Pathways from Carbon Monoxide and Hydrogen on the (0 0 1) Surface of the Iron Carbide χ-Fe5C2. *J. Catal.* **2015**, *325*, 9−18.
(60) Haw, J. F.; Marcus, D. M. Well-Defined (Supra)Molecular Structures in Zeolite Methanol-to-Olefin Catalysis. *Top. Catal.* **2005**, *34* (1−4), 41−48.
(61) Luo, M.; Zang, H.; Hu, B.; Wang, B.; Mao, G. Evolution of Confined Species and Their Effects on Catalyst Deactivation and Olefin Selectivity in SAPO-34 Catalyzed MTO Process. *RSC Adv.* **2016**, *6* (21), 17651−17658.
(62) Mohamed, H. O.; Parsapur, R. K.; Hita, I.; Cerrillo, J. L.; Ramírez, A.; Huang, K. W.; Gascon, J.; Castaño, P. Stable and Reusable Hierarchical ZSM-5 Zeolite with Superior Performance for Olefin Oligomerization When Partially Coked. *Appl. Catal., B* **2022**, *316*, 121582.
(63) Cordero-Lanzac, T.; Palos, R.; Hita, I.; Arandes, J. M.; Rodríguez-Mirasol, J.; Cordero, T.; Bilbao, J.; Castaño, P. Revealing the Pathways of Catalyst Deactivation by Coke during the Hydrodeoxygenation of Raw Bio-Oil. *Appl. Catal. B Environ.* **2018**, *239*, 513−524.
(64) Pena, J. A.; Monzon, A.; Santamaria, J. Deactivation by Coke of a Cr_2O_3/Al_2O_3 Catalyst During Butene Dehydrogenation. *J. Catal.* **1993**, *142* (1), 59−69.
(65) Royo, C.; Perdices, J. M.; Monzón, A.; Santamaría, J. Regeneration of Fixed-Bed Catalytic Reactors Deactivated by Coke: Influence of Operating Conditions and of Different Pretreatments of the Coke Deposits. *Ind. Eng. Chem. Res.* **1996**, *35* (6), 1813−1823.
(66) Takkawatakarn, T.; Praserthdam, S.; Wannakao, S.; Panpranot, J.; Praserthdam, P. Identification of Extremely Hard Coke Generation by Low-Temperature Reaction on Tungsten Catalysts via Operando and in Situ Techniques. *Sci. Rep.* **2021**, *11* (1), 8071.

https://doi.org/10.1021/acs.iecr.3c03956
Ind. Eng. Chem. Res. XXXX, XXX, XXX−XXX

(67) Zapater, D.; Lasobras, J.; Soler, J.; Herguido, J.; Menéndez, M. Comparison of Conventional and Two-Zone Fluidized Bed Reactors for Methanol to Olefins. Effect of Reaction Conditions and the Presence of Water in the Feed. *Ind. Eng. Chem. Res.* **2022**, *61* (17), 5757−5765.
(68) Lin, S.; Zhi, Y.; Zhang, W.; Yuan, X.; Zhang, C.; Ye, M.; Xu, S.; Wei, Y.; Liu, Z. Hydrogen Transfer Reaction Contributes to the Dynamic Evolution of Zeolite-Catalyzed Methanol and Dimethyl Ether Conversions: Insight into Formaldehyde. *Chin. J. Catal.* **2023**, *46*, 11−27.
(69) Sánchez del Campo, A. E.; Gayubo, A. G.; Aguayo, A. T.; Tarrío, A.; Bilbao, J. Acidity, Surface Species, and Mechanism of Methanol Transformation into Olefins on a SAPO-34. *Ind. Eng. Chem. Res.* **1998**, *37* (6), 2336−2340.
(70) Aguayo, A. T.; Gayubo, A. G.; Atutxa, A.; Olazar, M.; Bilbao, J. Regeneration of a Catalyst Based on a SAPO-34 Used in the Transformation of Methanol into Olefins. *J. Chem. Technol. Biotechnol.* **1999**, *74* (11), 1082−1088.
(71) Aguayo, A. T.; Gayubo, A. G.; Vivanco, R.; Olazar, M.; Bilbao, J. Role of Acidity and Microporous Structure in Alternative Catalysts for the Transformation of Methanol into Olefins. *Appl. Catal., A* **2005**, *283* (1−2), 197−207.
(72) Yang, M.; Fan, D.; Wei, Y.; Tian, P.; Liu, Z. Recent Progress in Methanol-to-Olefins (MTO) Catalysts. *Adv. Mater.* **2019**, *31* (50), 1902181.
(73) Guo, L.; Xing, A.; Zhu, W.; Li, F.; Guo, Z. Enhanced Methanol-To-Olefins (MTO) Performance over SAPO-34 Molecular Sieves Synthesized Using Novel Sources of Silicon and Aluminium. *Clean Energy* **2022**, *6* (3), 528−533.
(74) Wang, N.; Zhi, Y.; Wei, Y.; Zhang, W.; Liu, Z.; Huang, J.; Sun, T.; Xu, S.; Lin, S.; He, Y.; Zheng, A.; Liu, Z. Molecular Elucidating of an Unusual Growth Mechanism for Polycyclic Aromatic Hydrocarbons in Confined Space. *Nat. Commun.* **2020**, *11* (1), 1079.
(75) Luo, M.; Hu, B.; Mao, G.; Wang, B. Trace Compounds Confined in SAPO-34 and a Probable Evolution Route of Coke in the MTO Process. *ACS Omega* **2022**, *7* (4), 3277−3283.
(76) Arstad, B.; Nicholas, J. B.; Haw, J. F. Theoretical Study of the Methylbenzene Side-Chain Hydrocarbon Pool Mechanism in Methanol to Olefin Catalysis. *J. Am. Chem. Soc.* **2004**, *126* (9), 2991−3001.
(77) Svelle, S.; Joensen, F.; Nerlov, J.; Olsbye, U.; Lillerud, K. P.; Kolboe, S.; Bjørgen, M. Conversion of Methanol into Hydrocarbons over Zeolite H-ZSM-5: Ethene Formation Is Mechanistically Separated from the Formation of Higher Alkenes. *J. Am. Chem. Soc.* **2006**, *128* (46), 14770−14771.
(78) Yu, B.; Lou, C.; Zhang, W.; Xu, S.; Han, J.; Yu, Z.; Wei, Y.; Liu, Z. Insight into the Dual Cycle Mechanism of Methanol-to-Olefins Reaction over SAPO-34 Molecular Sieve by Isotopic Tracer Studies. *Chem. Res. Chin. Univ.* **2020**, *36* (6), 1203−1208.
(79) Gao, M.; Li, H.; Liu, W.; Xu, Z.; Peng, S.; Yang, M.; Ye, M.; Liu, Z. Imaging Spatiotemporal Evolution of Molecules and Active Sites in Zeolite Catalyst during Methanol-to-Olefins Reaction. *Nat. Commun.* **2020**, *11* (1), 3641.

https://doi.org/10.1021/acs.iecr.3c03956
Ind. Eng. Chem. Res. XXXX, XXX, XXX−XXX